ACS Photonics

Article

pubs.acs.org/journal/apchd5

Simultaneous Multiharmonic Imaging of Nanoparticles in Tissues for Increased Selectivity

Andrii Rogov,[†] Marie Irondelle,[‡] Fernanda Ramos Gomes,[§] Julia Bode,[§] Davide Staedler,[†,⊥] Solène Passemard,[⊥] Sébastien Courvoisier,[†] Yasuaki Yamamoto,[∥] François Waharte,[‡] Daniel Ciepielewski,[#] Philippe Rideau,[⊗] Sandrine Gerber-Lemaire,[⊥] Frauke Alves,[§] Jean Salamero,[‡] Luigi Bonacina,*[,†] and Jean-Pierre Wolf[†]

[†]GAP-Biophotonics, Université de Genève, 22 Chemin de Pinchat, 1211 Genève, Switzerland

[‡]Cell and Tissue Imaging Facility (PICT-IBiSA), CNRS UMR144 Institut Curie, Paris 75248, France

[§]Department of Molecular Biology of Neuronal Signals, Max-Planck-Institute of Experimental Medicine, Hermann-Rein-Straße 3, 37075 Göttingen, Germany

[⊥]Laboratory of Synthesis and Natural Products, Institute of Chemical Sciences and Engineering, École Polytechnique Fédérale de Lausanne, Batochime, 1015 Lausanne, Switzerland

[∥]JEOL SAS Espace Claude Monet, 1 Allee de Giverny, 78290 Croissy-sur-Seine, France

[#]Nikon AG - Instruments, Im Hanselmaa 10, 8132 Egg/ZH, Switzerland

[⊗]Nikon France & BeLux - Division Instruments, 191 Rue du Marché Rollay, 94504 Champigny sur Marne, France

Supporting Information

ABSTRACT: We investigate the use of bismuth ferrite (BFO) nanoparticles for tumor tissue labeling in combination with infrared multiphoton excitation at 1250 nm. We report the efficient and simultaneous generation of second- and third-harmonic signals by the nanoparticles. On this basis, we set up a novel imaging protocol based on the co-localization of the two harmonic signals and demonstrate its benefits in terms of increased selectivity against endogenous background sources in tissue samples. Finally, we discuss the use of BFO nanoparticles as mapping reference structures for correlative light−electron microscopy.

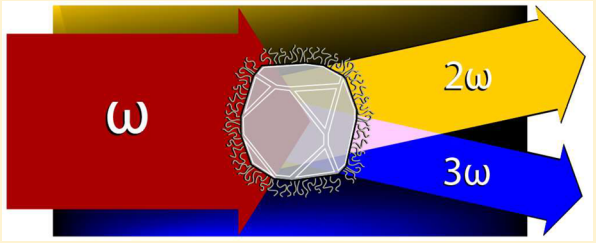

KEYWORDS: *second-harmonic generation, third-harmonic generation, nanoparticles, tissue imaging, multiphoton microscopy*

The advent of multiphoton microscopy in the early 1990s has revolutionized the field of optical imaging.[1] This technique has proven particularly beneficial for biological studies. Nowadays, thanks to the availability of compact ultrafast sources exceeding the traditional 700−1000 nm range of Ti:sapphire oscillators and covering the spectral region up to 1300 nm, the way is paved for improved performances in terms of imaging penetration and novel applications for tissue diagnostics and tumor invasion studies.[2] The tunability of these sources allows selecting the excitation wavelength for minimizing water absorption and scattering according to sample characteristics.[3,4] Traditional nanophotonics labeling approaches (quantum dots, plasmonic nanoparticles (NPs), up-conversion NPs) display fixed optical properties often in the UV−visible spectral region and cannot fully take advantage of this spectral extension. To circumvent wavelength limitations, a few research groups in the last years have introduced a new nanotechnological approach based on metal oxide nanocrystals with noncentrosymmetric lattice, harmonic nanoparticles (HNPs).[5−7] By their crystalline structure, HNPs present very efficient nonlinear $\chi^{(2)}$ response and can be effectively imaged using second harmonic (SH) emission as a contrast mechanism efficiently responding to excitation from the UV to the mid-IR.[8] Moreover their signal is not bleaching, blinking, nor saturating because of the nonresonant character of the photointeraction mechanism involved.[9,10] Multiharmonic emission by HNPs has already been sparsely reported to date.[8,11,12] Extermann et al. first observed third-harmonic (TH) generation in $Fe(IO_3)_3$ HNPs by exciting at 1500 nm with an SH/TH intensity ratio of approximately 100.[8]

In this work, we use 100−120 nm diameter bismuth ferrite (BFO) HNPs with a poly(ethylene glycol) (PEG) biocompatible coating prepared for further functionalization (see the SI, section 1.1). BFO HNPs have been recently presented as the most promising candidates for translating HNPs to medical applications. In fact, they present a very high second-order nonlinear coefficient, $\langle d \rangle = 79$ pm/V[13] (for comparison $\langle d \rangle \approx 4$

Received: February 11, 2015
Published: September 29, 2015

DOI: 10.1021/acsphotonics.5b00289
ACS Photonics 2015, 2, 1416−1422

pm/V for $BaTiO_3$ and $KNbO_3$ HNPs),[14] and extremely good biocompatibility, in particular when PEG-coated. A thorough discussion about the effect of PEG-coated BFO HNPs on various cancer and healthy cell lines has been recently published.[15] In this reference, the effects of BFO HNPs in terms of cell viability, membrane permeability, lysosomal mass, intracellular localization, and hemolytic potential are assessed by high-throughput methods at different concentrations and for several incubation times. Recently, BFO HNPs have been applied with success to novel *in vitro* applications in cancer research and regenerative medicine. Apart from polymer coating for increased biocompatibility, the functionalization of HNPs for specific targeting has been demonstrated for $BaTiO_3$.[16−18]

For optical nonlinear imaging we employed a Nikon A1R multiphoton upright microscope (NIE-Nikon) coupled with an Insight Deepsee tunable laser oscillator (Spectra-Physics, 120 fs, 80 MHz, 680−1300 nm). With respect to standard systems based on Ti:sapphire oscillators, the microscope was optimized for infrared transmission using tailored reflection coatings and dedicated transmission components. The nonlinear signals were epi-collected by two different long working distance objectives (25× CFI75 APO NA 1.1 and 16× CFI75 NA 0.8) spectrally filtered by tailored pairs of dichroic mirrors and interference filters and acquired in parallel either by a standard photomultiplier (600−655 nm) or by a GaAsP photomultiplier (385−492 nm).

The top-left plot in Figure 1 shows the SH emission at 625 nm generated by BFO HNPs deposited on a substrate when excited at 1250 nm. The intensity differences among HNPs in the image reflect their size dispersion and crystal axis orientation with respect to the polarization of the excitation laser.[20] When detecting at the TH frequency (416 nm), HNPs also appear very bright. We have applied to this two-color image the algorithm developed by Costes et al. to detect co-localized SH/TH events.[19] This recognized computational method has the advantage of automatically determining the signal thresholds for both detection channels with no user bias. Any event in the region above the two thresholds (T_{SH} and T_{TH}) indicated by the two thick lines parallel to the axes is assumed as co-localized, and the associated pixels appear white in the SH∩TH plot. One can see that this region encompasses the quasi-totality of the nanoparticles on the substrate. The diagonal line in the scatter plot is automatically determined by the algorithm as a result of a linear regression of the whole data set. The dispersion of the data points around this reference line is not surprising: a strict linear dependence between the two normalized harmonic signals is not expected, because of their different intensity dependence ($\propto I^2$ and $\propto I^3$, respectively for SH and TH) and of other factors influencing differently the two emissions, e.g., orientation. More importantly, a constant ratio between TH and SH by HNPs *is not required* for the co-localization procedure to work. By running a test of significance, we obtain a *P*-value of 1.0, indicating that all the events identified by the algorithm as co-localized are truly so from a statistical standpoint.[21,22] For a comparison, the widely used (but less informative) Pearson coefficient obtained for this data set is 0.87. Importantly, such multiharmonic emission is not limited to BFO HNPs, although for this material the ratio seems particularly favorable. In SI section 2.3, we report the results obtained using a different HNP material ($KNbO_3$) as an additional demonstration of the procedure.

The normalized power dependence measured on a single BFO HNP for both SH and TH with the characteristic I^2 and I^3 dependence is reported in Figure 2A with the corresponding exponential fit confirming their assignment (1.95 and 3.2 for SH and TH, respectively). As expected, the SH/TH ratio changes according to excitation intensity, and indeed Dai et al. have recently investigated this dependence in ZnO NPs for prospective applications in display technology.[12] By calibrating the spectral transmission of optics and response of the detectors, we could estimate the SH/TH BFO intensity ratio to a factor 40 to 100 at 1250 nm, depending on the intensity applied. A detailed description of the procedures used for this estimate can be found in SI section 2.1. In SI section 2.2 we also present a calculation of the expected emission anisotropy as a function of particle size, indicating that within the particle dimension range used in this work no destructive interference

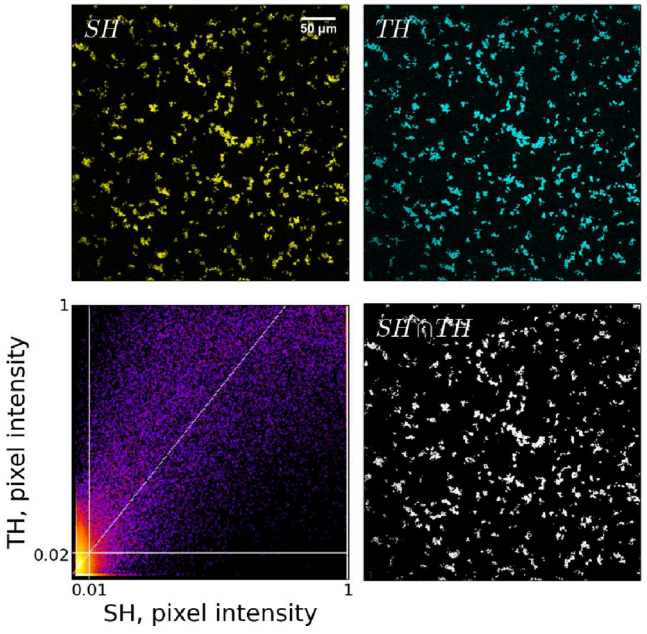

Figure 1. Multiharmonic emission by bare BFO HNPs deposited on a substrate. SH: Second-harmonic image. TH: Third-harmonic image. Scatter plot: TH vs SH pixel intensity. The lines parallel to the axes indicate the threshold levels determined by the Costes algorithm;[19] events with intensities greater than both thresholds are considered co-localized. The diagonal line is a linear fit to the whole data set. SH∩TH: Co-localization image with co-localized pixels in white. Pixel size: 0.79 μm, PSF not oversampled.

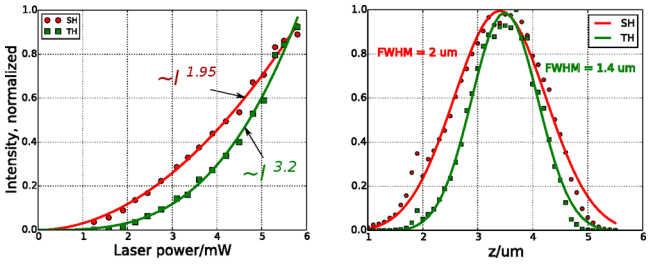

Figure 2. (A) SH and TH power dependence measured on an individual BFO HNP. Markers: Experimental values. Thick lines: I^n fits yielding n = 1.95 and 3.2 for SH and TH, respectively. (B) Nonlinear axial PSF at SH and TH obtained with a 1.1 NA objective and 1250 nm excitation. Markers: Experimental values. Thick lines: Gaussian fits yielding fwhm = 1.97 and 1.42 μm for SH and TH, respectively.

DOI: 10.1021/acsphotonics.5b00289
ACS Photonics 2015, 2, 1416−1422

effects are expected for the epi-detected fraction of both SH and TH emission. In Figure 2B, we show how the nonlinear axial point spread functions (PSF) measured at the second and third order on a single subdiffraction-limited HNP are different. Because of higher nonlinearity order, the TH PSF is narrower, leading to increased resolution, an aspect that might turn out to be particularly beneficial when working at long wavelengths.[23]

Although a large $\chi^{(3)}$ response is not surprising for large $\chi^{(2)}$ samples,[24] the simultaneous collection of multiple harmonics by excitation-tunable nanometric systems can be very advantageous for increasing selectivity in demanding applications, such as ultrasensitive detection in fluids, as recently demonstrated.[25] For imaging, the use of >1100 nm excitation wavelengths ensures that standard microscope collection optics and acquisition detectors can be efficiently employed at the TH frequency. The two harmonic signals are very well spectrally separated and characterized by narrow bandwidths, which make them easily distinguishable also when using conventional fluorescence filters for detection.

To investigate the advantages of multiharmonic detection in relevant biomedical samples, we proceeded in imaging excised cancer tissues from a xenograft tumor model. Details of preparation are provided in SI sections 1.3 and 1.4. Briefly, we analyzed tumors developed in female nude mice after implantation of human breast tumor cells MDA MB 231 either subcutaneously or orthotopically in the right abdominal mammary gland fat pad. Fresh breast tumor tissue sections were obtained using a vibratome, followed by incubation either with BFO HNPs or in buffer as a control.

In Figure 3 we show a multiharmonic image of an unlabeled section from the breast orthotopic tumor (negative control). It

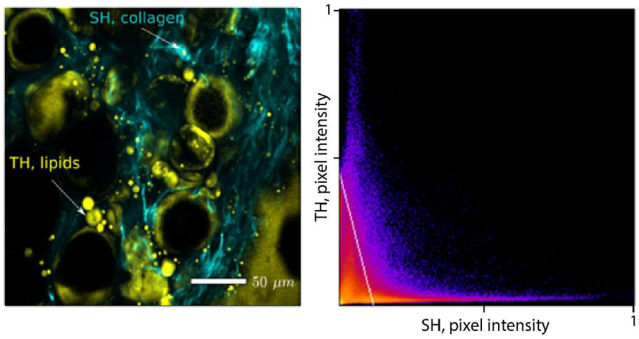

Figure 3. Left: Representative multiphoton image of an unlabeled tissue section of an orthotopic breast tumor. Cyan: SH. Yellow: TH. Right. Scatter plot of TH vs SH. The algorithm indicates no positive events for co-localization (the diagonal line with negative slope points to anti-co-localization; the Pearson's coefficients is −0.09). Pixel size: 0.65 μm, PSF not oversampled.

is known that strong endogenous sources of second- (cyan, collagen)[26] and third-harmonic (yellow, lipids)[27] signals exist in tissues. Both these tissue constituents are abundant in tumors[2,28−30] and are clearly present in the picture. Such harmonic background can affect the selective detection of HNPs. Some authors have already shown that HNPs can be imaged by their SH emission against a collagen background (mammalian tendon).[10,31] However, it was also shown that for individual HNPs the contrast was reduced,[31] even though instrumental sensitivity was sufficient for detecting single HNP emission. Interestingly, the application of Costes's algorithm fails on this image slice because of the almost total absence of co-localization events to perform the computation. This finding is consistent with the distribution of pixels in the scatter plot, where elements yielding simultaneously high SH and TH are sorely missing. The calculation of Pearson's coefficient for this image yields a negative value (−0.09).

The first column of Figure 4 displays the SH signal of a tissue section from the subcutaneous breast tumor which was incubated with BFO HNPs. Collagen structures are clearly evident as diagonal stripes; the presence of small bright spots (sometimes at the limit of pixel resolution) is more pronounced than in the negative control of Figure 3 and points to the presence of HNPs in the sample. Likewise, the TH image in the central row shows the presence of small spots, together with other larger structures with different morphology with respect to collagen, which can be ascribed to lipids.[2,29] The results of the co-localization procedure (SH∩TH, rightmost plot) enables highlighting in white exclusively pixels that show a simultaneous multiharmonic emission and that, on the basis of the findings discussed in relation to Figures 1 and 3, can be safely associated with the presence of BFO HNPs. The second row of Figure 4 provides a more quantitative analysis of this co-localization effect. The semilog histograms of pixel intensity at both the SH and TH cover the whole detection dynamic range. Co-localization bars (in blue) indicate the number of occurrences that can be simultaneously attributed to both harmonic channels. One can see that the discrimination of the HNP signal against background emission of endogenous sources cannot be based simply on intensity, as in both detection channels a relevant fraction of events at high intensity are not co-localizing. When comparing the intensity emitted by endogenous structures with that of HNPs, one has to take into account that the former despite their lower nonlinear efficiency (e.g., $\langle d \rangle$ = 0.94 pm/V for collagen[32]) are generally characterized by much larger dimensions (fulfilling or exceeding the focal volume); therefore the squared-volume dependence of harmonic signals can easily counteract the harmonic generation efficiency difference.

We cannot exclude that a few low-intensity multiharmonic positive events are not accounted for by the algorithm as inevitable in the case of automatic image analysis.[19] On the other hand, false positive detections seem unlikely. Although we used relatively broadband fluorescence filters as compared to the narrow SH and TH emission bandwidths, we carefully ensured that no autofluorescence is emitted upon two- and three-photon absorption when working at 1200 nm with the excitation settings employed here (for a complete analysis refer to SI section 3). Clearly, a preliminary assessment of the anti-co-localization of endogenous sources in a negative control sample (Figure 3 in the present case) is mandatory for the success of the approach.

The application of multiharmonic correlation for increasing selectivity by background rejection in an optically congested environment such as tissues can be performed in real time and, therefore, opens the way to HNP tracking protocols[33,34] with high selectivity and minimal image processing requirements. Moreover, autofluorescence can be minimized when working in this wavelength range, avoiding endogenous fluorophores such as riboflavins and NADH, which display two-photon absorption bands peaked at wavelengths of <1000 nm.[23] In addition, it is worth noting that resolution is generally not an issue for detecting HNPs. As demonstrated by the Beaurepaire group, it is advantageous when imaging thick samples by multiphoton excitation to employ objectives with low magnification and

DOI: 10.1021/acsphotonics.5b00289
ACS Photonics 2015, 2, 1416−1422

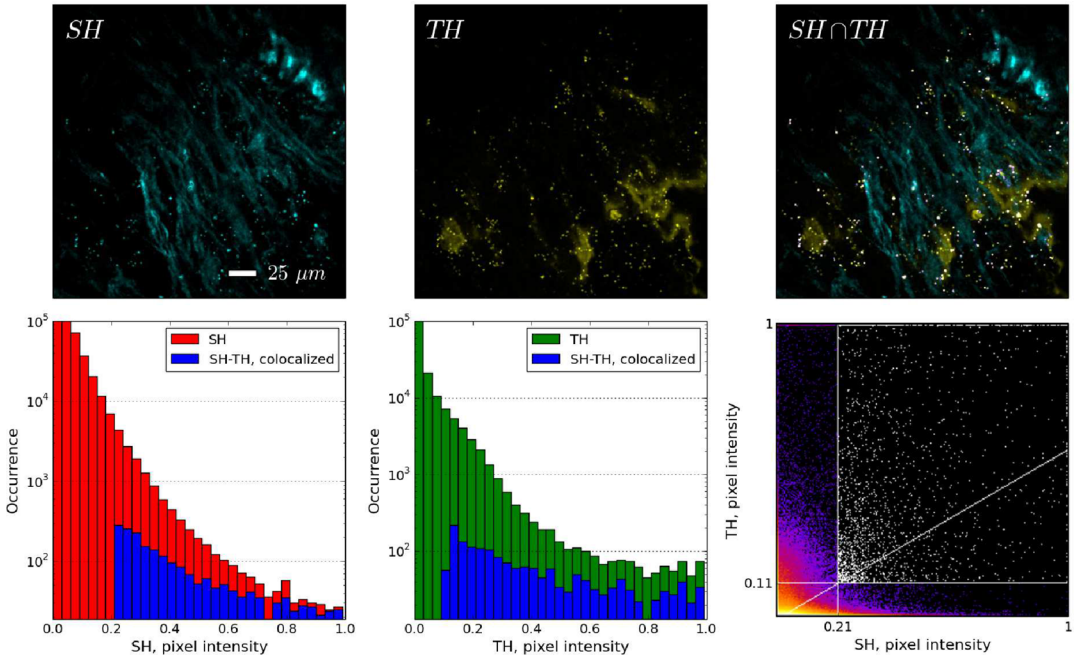

Figure 4. Representative multiphoton images of subcutaneous breast tumor tissue labeled with BFO HNPs. First row: SH (cyan), TH (yellow), and SH∩TH merged image with co-localized pixels in white. Second row: Semilog SH and TH intensity histograms. Blue bars correspond to co-localized events. Scatter plot: TH vs SH. As in Figure 1, the lines parallel to the axes indicate the automatically determined threshold values, and the diagonal line is a linear fit to the whole data set. Only the events above the thresholds (white pixels) are assumed as co-localized. Pixel size: 0.65 μm, PSF not oversampled.

large field of view/NA to epi-collect efficiently multiple scattered photons.[35]

The measurements presented were performed with peak pulse intensity at the sample going from 300 to 650 GW/cm^2. Even by assuming the highest of these two values (calculated in the femtosecond regime and corresponding to a 16 mW average laser power) and considering the scanning speed used for raster imaging, which corresponds to a pulse density of 1.2 $\times$ 10^3 μm^{-2},[36] we can calculate that these conditions are suitable for imaging of biological samples. Indeed these figures are sensibly lower than the photoinduced tissue damage threshold established by Supatto et al. on living drosophila embryos.[36] As a further assessment, the highly cited paper by Köning on cellular response to near-infrared femtosecond excitation sets a damage threshold on cell viability and reproduction at 1 TW/cm^2.[37] Although we approach this intensity value in absolute terms, it should be noted that this estimate was derived at a shorter wavelength (730−800 nm instead of >1200 nm), implying a lower order multiphoton process for absorption by endogenous molecules and at a much longer dwell time (80 μs as compared to 4 μs here).

To further assess the actual penetration limits of the proposed HNP-based multiharmonic imaging protocol, we have simulated the optical response of an HNP embedded at depth z in a tissue and calculated the theoretical epi-detected signals. This numerical analysis aims at determining how the TH/SH ratio obtained at the uppermost surface of a three-dimensional z-stack is modified upon penetration in the tissue. Simulations are based on a free-ware C-code for light propagation[38,39] that we modified to account for nonlinear excitation. We assume that a 1200 nm input beam is focused by a NA 0.8, 3 mm WD objective in two different kinds of tissue slabs (rat liver and ear cartilage) characterized by the sets of optical properties ($\mu_a(\lambda)$, $\mu_s(\lambda)$, $g(\lambda)$) reported in SI section 5.[40] The simulation volume is composed by 700^3 voxels of 7 μm side. The HNP placed at the focus is assumed to irradiate isotropically at the SH and TH with an efficiency depending respectively on the local I^2 and I^3 excitation intensity. We then calculate the fraction of SH and TH photons emitted by the HNP reaching the objective and, from these values, the TH/SH value. This ratio is assumed to be 1 at the entrance surface. In the lower plot of Figure 5, one can observe an exponential decrease of the TH/SH ratio as a function of depth z. The observed decrease is more prominent for liver than for ear cartilage, consistently with the higher scattering and absorption at the TH wavelength for the former tissue. This finding can be appreciated in the series of images on the right in Figure 5, reporting the normalized focal intensity and emission patterns for an HNP embedded at 300 μm depth in a liver tissue. As sketched in the top panel, the upper side of each image corresponds to the objective lens and the red dotted lines are the focusing beam. The horizontal dashed line defines the position of the tissue surface. Comparing the SH and TH emission patterns, one can see how the penetration of TH in the tissue is strongly limited by absorption as compared to SH. As a general trend, we can deduce that for these two representative tissues the initial TH/SH ratio drops to its 1/e value within the 100−200 μm range. On the basis of the fact that the co-localization algorithm does not require a fixed ratio and that we could roughly co-localize events with TH/SH variations within 1 order of magnitude (see scatter plot in Figure 1), for a given set of detection parameters, we can extrapolate a working range of approximately 300 μm in a cartilage kind of tissue and approximately 200 μm in the optically more extreme liver case. These values are compatible with the requirements of many cell tracking applications.

In light of previous results, an interesting development for the use of HNPs for tissue imaging is their application as

DOI: 10.1021/acsphotonics.5b00289
ACS Photonics 2015, 2, 1416−1422

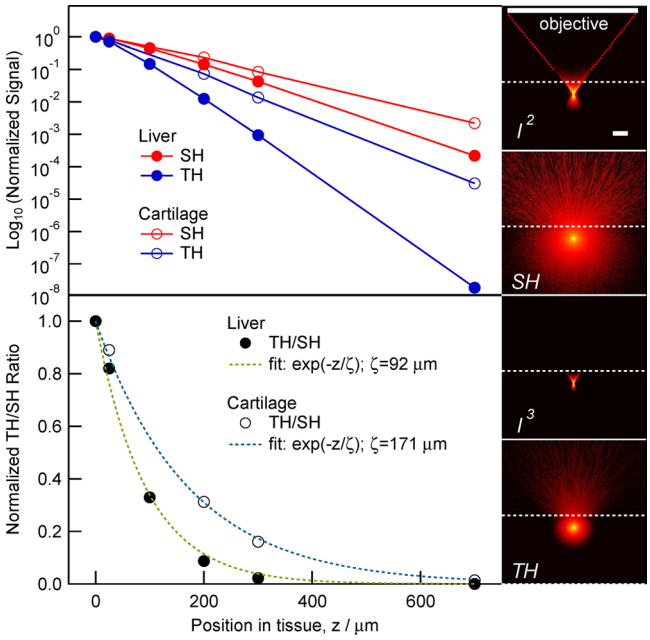

Figure 5. Results of Monte Carlo light transport simulations. Upper plot: Normalized detected SH and TH signals (semilog scale) as a function of HNP position z for two relevant tissue types: liver and cartilage. Lower plot: Normalized TH/SH ratio calculated from the same data set. Right panels: Two-dimensional slices of the simulation volume in the case of an HNP embedded at z = 300 μm in the liver, reporting from top to bottom: the excitation intensity squared, the SH emission pattern, the excitation intensity cubed, and the TH emission pattern. The upper side of each image corresponds to the objective aperture; the dashed line indicates the position of tissue surface. The intensity logarithmic colormaps are conserved between focal intensity plots (spanning 5 orders of magnitude) and TH/SH emission plots (7 orders of magnitude), allowing a direct comparison.

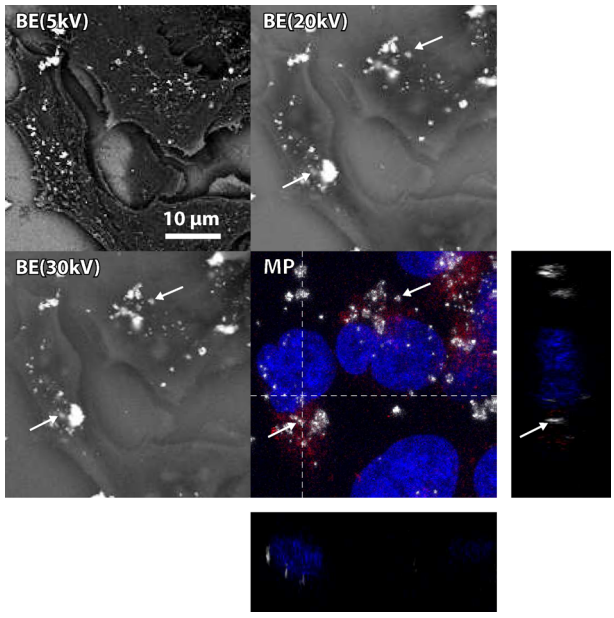

Figure 6. Demonstration of CLEM imaging of MDA MB 231 cells labeled by BFO HNPs. BE: Secondary electron SEM images at 5, 20, and 30 kV. MP: Multiphoton maximal intensity projection image with two vertical cuts corresponding to the dashed lines. Red: Nile Red fluorescence staining lipids (membranes). Blue: DAPI fluorescence (nuclei). White: SH by HNPs. Arrows indicate throughout the different images two exemplary clusters appearing only at high SEM voltages (20 and 30 kV).

reference mapping structures for correlating light (multiphoton) and electron microscopy (CLEM), facilitating the retrieval of specific regions of interest (ROI) going from one technique to the other.[41] In this respect, BFO HNPs are particularly appealing, as they are electron dense and are expected to provide good contrast in electron-based imaging such as TEM and SEM. Figure 6 shows a SEM representative image, including several cells imaged at different voltages in backscattered electron (BE) mode. BEs (>50 eV) are preferable in this case, as they are known to be sensitive to the composition of the specimen and display brighter contrast for heavier elements. Overall, one can notice the good contrast provided by SEM for BFO HNPs. By changing accelerating voltage one can modify the scattering region of the incident electron beam (SI section 6). While the 5 kV image reports details of the cell's surface and indicates the presence of individual particles or small HNPs clusters, when the SEM voltage is increased to 20 and 30 kV, larger aggregates located below the cell surface appear as indicated by the arrows. The presence and position of these aggregates correlate well with previous studies indicating that BFO HNPs initially adhere to the cell membrane (2 h), are successively internalized with increasing exposure time, and tend to concentrate in intracellular organelles, such as endosomes or lysosomes.[15] Finally, panel MP shows a maximal intensity projection image of the same ROI imaged by multiphoton microscopy.

In this case, fluorescent labels were used to stain nuclei (DAPI, blue) and lipids such as cell membranes (Nile Red, red). SH from HNPs appears in white. One can see that HNPs tend to localize at the membranes, in particular in a region with higher density subcellular membrane compartments where they are thicker (red intensity higher). Two vertical projections corresponding to the sections indicated by the dashed lines are also reported. Within the optical resolution, they indicate that HNPs are mainly located inside the membranes or at cell upper surfaces, confirming an already observed tendency to avoid the nuclear region and co-localize in lysosomes or at the cell surface.[15]

In conclusion, we have shown that multiharmonic emission of BFO HNPs can be easily detected by multiphoton microscopy when using excitation of >1100 nm. Very advantageously, the intensity difference among second and third nonlinear response is not large. Using the right combination of detectors for the different spectral ranges (GaAsP and standard photomultipliers) the two signals can be acquired simultaneously using standard settings. On the basis of this result, we have demonstrated that the co-localization of SH and TH allow identifying with high selectivity HNPs in a complex optical environment presenting endogenous sources of fluorescence and harmonic generation an excised xenograft tumor tissue in our experiment. The image processing necessary for this approach relies on simple two-channel co-localization, allowing its real-time use in demanding imaging applications. Numerical simulations of light transport indicate that the proposed imaging protocol can be performed up to a thickness of a few hundred micrometers, which are relevant length scales for cell tracking applications. Moreover, by additional electron microscopy measurements, we have shown that BFO HNPs could prospectively serve as localization fiduciaries in advanced CLEM studies.[42]

DOI: 10.1021/acsphotonics.5b00289
ACS Photonics 2015, 2, 1416−1422

■ ASSOCIATED CONTENT

Supporting Information

The Supporting Information is available free of charge on the ACS Publications website at DOI: 10.1021/acsphotonics.5b00289.

Additional details on the experimental procedures (PDF)

■ AUTHOR INFORMATION

Corresponding Author

*E-mail: luigi.bonacina@unige.ch.

Notes

The authors declare the following competing financial interest(s): One of the authors of the paper (D. Staedler) has started commercializing harmonic nanoparticles of different materials through his company TiBio since 2015.

■ ACKNOWLEDGMENTS

This research was partially supported by the European FP7 Research Project NAMDIATREAM (NMP4-LA-2010-246479, http://www.namdiatream.eu), Fondation pour la Recherche Médicale (FRM n. DGE20111123020), and the Cancéropôle Ile de France (n. 2012-2-EML-04-IC-1, 246479, http://www.namdiatream.eu). The financial support by the NCCR Molecular Ultrafast Science and Technology (NCCR MUST), a research instrument of the Swiss National Science Foundation (SNSF), is also acknowledged. The study was performed in the context of the European COST Action MP1302 Nanospectroscopy. GAP-Biophotonics authors are grateful to Michel Moret for technical support.

■ REFERENCES

(1) Denk, W.; Strickler, J. H.; Webb, W. W. Two-photon laser scanning fluorescence microscopy. *Science* **1990**, *248*, 73−76.

(2) Weigelin, B.; Bakker, G.-J.; Friedl, P. Intravital third harmonic generation microscopy of collective melanoma cell invasion: principles of interface guidance and microvesicle dynamics. *Intravital* **2012**, *1*, 32−43.

(3) Andresen, V.; Alexander, S.; Heupel, W.-M.; Hirschberg, M.; Hoffman, R. M.; Friedl, P. Infrared multiphoton microscopy: subcellular-resolved deep tissue imaging. *Curr. Opin. Biotechnol.* **2009**, *20*, 54−62.

(4) Horton, N. G.; Wang, K.; Kobat, D.; Clark, C. G.; Wise, F. W.; Schaffer, C. B.; Xu, C. In vivo three-photon microscopy of subcortical structures within an intact mouse brain. *Nat. Photonics* **2013**, *7*, 205−209.

(5) Nakayama, Y.; Pauzauskie, P. J.; Radenovic, A.; Onorato, R. M.; Saykally, R. J.; Liphardt, J.; Yang, P. D. Tunable nanowire nonlinear optical probe. *Nature* **2007**, *447*, 1098−U8.

(6) Dempsey, W. P.; Fraser, S. E.; Pantazis, P. SHG nanoprobes: Advancing harmonic imaging in biology. *BioEssays* **2012**, *34*, 351−360.

(7) Bonacina, L. Nonlinear Nanomedecine: Harmonic Nanoparticles toward Targeted Diagnosis and Therapy. *Mol. Pharmaceutics* **2013**, *10*, 783−792.

(8) Extermann, J.; Bonacina, L.; Cuna, E.; Kasparian, C.; Mugnier, Y.; Feurer, T.; Wolf, J. P. Nanodoublers as deep imaging markers for multi-photon microscopy. *Opt. Express* **2009**, *17*, 15342−15349.

(9) Le Xuan, L.; Zhou, C.; Slablab, A.; Chauvat, D.; Tard, C.; Perruchas, S.; Gacoin, T.; Villeval, P.; Roch, J. F. Photostable second-harmonic generation from a single KTiOPO4 nanocrystal for nonlinear microscopy. *Small* **2008**, *4*, 1332−1336.

(10) Pantazis, P.; Maloney, J.; Wu, D.; Fraser, S. E. Second harmonic generating (SHG) nanoprobes for in vivo imaging. *Proc. Natl. Acad. Sci. U. S. A.* **2010**, *107*, 14535−14540.

(11) Cai, F.; Yu, J.; Qian, J.; Wang, Y.; Chen, Z.; Huang, J.; Ye, Z.; He, S. Use of tunable second harmonic signal from $KNbO_3$ nanoneedles to find optimal wavelength for deep tissue imaging. *Laser Photonics Rev.* **2014**, *8*, 865.

(12) Dai, J.; Yuan, M.-H.; Zeng, J.-H.; Dai, Q.-F.; Lan, S.; Xiao, C.; Tie, S.-L. Controllable color display induced by excitation-intensity-dependent competition between second and third harmonic generation in ZnO nanorods. *Appl. Opt.* **2014**, *53*, 189−194.

(13) Schwung, S.; Rogov, A.; Clarke, G.; Joulaud, C.; Magouroux, T.; Staedler, D.; Passemard, S.; Justel, T.; Badie, L.; Galez, C. Nonlinear optical and magnetic properties of $BiFeO_3$ harmonic nanoparticles. *J. Appl. Phys.* **2014**, *116*, 114306.

(14) Staedler, D.; et al. Harmonic Nanocrystals for Biolabeling: A Survey of Optical Properties and Biocompatibility. *ACS Nano* **2012**, *6*, 2542−2549.

(15) Staedler, D.; et al. Cellular Uptake and Biocompatibility of Bismuth Ferrite Harmonic Advanced Nanoparticles. *Nanomedicine* **2015**, *11* (4), 815−828.

(16) Hsieh, C. L.; Grange, R.; Pu, Y.; Psaltis, D. Bioconjugation of barium titanate nanocrystals with immunoglobulin G antibody for second harmonic radiation imaging probes. *Biomaterials* **2010**, *31*, 2272−2277.

(17) Culić-Viskota, J.; Dempsey, W. P.; Fraser, S. E.; Pantazis, P. Surface functionalization of barium titanate SHG nanoprobes for in vivo imaging in zebrafish. *Nat. Protoc.* **2012**, *7*, 1618−1633.

(18) Liu, J.; Cho, I.-H.; Cui, Y.; Irudayaraj, J. Second Harmonic Super-Resolution Microscopy for Quantification of mRNA at Single Copy Sensitivity. *ACS Nano* **2014**, *8*, 12418−12427.

(19) Costes, S. V.; Daelemans, D.; Cho, E. H.; Dobbin, Z.; Pavlakis, G.; Lockett, S. Automatic and quantitative measurement of protein-protein colocalization in live cells. *Biophys. J.* **2004**, *86*, 3993−4003.

(20) Bonacina, L.; Mugnier, Y.; Courvoisier, F.; Le Dantec, R.; Extermann, J.; Lambert, Y.; Boutou, V.; Galez, C.; Wolf, J. P. Polar Fe(IO3)(3) nanocrystals as local probes for nonlinear microscopy. *Appl. Phys. B: Lasers Opt.* **2007**, *87*, 399−403.

(21) Lifshitz, L. M. Determining data independence on a digitized membrane in three dimensions. *IEEE T. Med. Imaging* **1998**, *17*, 299−303.

(22) Schindelin, J.; Arganda-Carreras, I.; Frise, E.; Kaynig, V.; Longair, M.; Pietzsch, T.; Preibisch, S.; Rueden, C.; Saalfeld, S.; Schmid, B. Fiji: an open-source platform for biological-image analysis. *Nat. Methods* **2012**, *9*, 676−682.

(23) Zipfel, W. R.; Williams, R. M.; Christie, R.; Nikitin, A. Y.; Hyman, B. T.; Webb, W. W. Live tissue intrinsic emission microscopy using multiphoton-excited native fluorescence and second harmonic generation. *Proc. Natl. Acad. Sci. U. S. A.* **2003**, *100*, 7075−7080.

(24) Morita, R.; Yamashita, M. Relationship between 2nd-Order and 3rd-Order Nonlinear-Optical Susceptibilities Due to Electronic Polarization. *Jpn. J. Appl. Phys. 2* **1993**, *32*, L905−L907.

(25) Geissbuehler, M.; Bonacina, L.; Shcheslavskiy, V.; Bocchio, N. L.; Geissbuehler, S.; Leutenegger, M.; Marki, I.; Wolf, J. P.; Lasser, T. Nonlinear Correlation Spectroscopy (NLCS). *Nano Lett.* **2012**, *12*, 1668−1672.

(26) Williams, R. M.; Zipfel, W. R.; Webb, W. W. Interpreting second-harmonic generation images of collagen I fibrils. *Biophys. J.* **2005**, *88*, 1377−1386.

(27) Débarre, D.; Supatto, W.; Pena, A.-M.; Fabre, A.; Tordjmann, T.; Combettes, L.; Schanne-Klein, M.-C.; Beaurepaire, E. Imaging lipid bodies in cells and tissues using third-harmonic generation microscopy. *Nat. Methods* **2006**, *3*, 47−53.

(28) Shoulders, M. D.; Raines, R. T. Collagen structure and stability. *Annu. Rev. Biochem.* **2009**, *78*, 929.

(29) Le, T. T.; Huff, T. B.; Cheng, J.-X. Coherent anti-Stokes Raman scattering imaging of lipids in cancer metastasis. *BMC Cancer* **2009**, *9*, 42.

(30) Kakkad, S. M.; Solaiyappan, M.; Argani, P.; Sukumar, S.; Jacobs, L. K.; Leibfritz, D.; Bhujwalla, Z. M.; Glunde, K. Collagen I fiber density increases in lymph node positive breast cancers: pilot study. *J. Biomed. Opt.* **2012**, *17*, 116017−116017.

DOI: 10.1021/acsphotonics.5b00289
ACS Photonics 2015, 2, 1416−1422

(31) Grange, R.; Lanvin, T.; Hsieh, C. L.; Pu, Y.; Psaltis, D. Imaging with second-harmonic radiation probes in living tissue. *Biomed. Opt. Express* **2011**, *2*, 2532−2539.
(32) Stoller, P.; Celliers, P. M.; Reiser, K. M.; Rubenchik, A. M. Quantitative second-harmonic generation microscopy in collagen. *Appl. Opt.* **2003**, *42*, 5209−5219.
(33) Magouroux, T.; Extermann, J.; Hoffmann, P.; Mugnier, Y.; Le Dantec, R.; Jaconi, M. E.; Kasparian, C.; Ciepielewski, D.; Bonacina, L.; Wolf, J.-P. High-Speed Tracking of Murine Cardiac Stem Cells by Harmonic Nanodoublers. *Small* **2012**, *8*, 2752−2756.
(34) Macias-Romero, C.; Didier, M. E. P.; Zubkovs, V.; Delannoy, L.; Dutto, F.; Radenovic, A.; Roke, S. Probing rotational and translational diffusion of nanodoublers in living cells on microsecond time scales. *Nano Lett.* **2014**, *14*, 2552−2557.
(35) Débarre, D.; Olivier, N.; Beaurepaire, E. Signal epidetection in third-harmonic generation microscopy of turbid media. *Opt. Express* **2007**, *15*, 8913−8924.
(36) Supatto, W.; Débarre, D.; Farge, E.; Beaurepaire, E. Femtosecond pulse-induced microprocessing of live Drosophila embryos. *Med. Laser Appl.* **2005**, *20*, 207−216.
(37) König, K.; So, P.; Mantulin, W.; Gratton, E. Cellular response to near-infrared femtosecond laser pulses in two-photon microscopes. *Opt. Lett.* **1997**, *22*, 135−136.
(38) Jacques, S. http://omlc.org/software/mc/mcxyz/, 2014.
(39) Wang, L.; Jacques, S. L.; Zheng, L. MCML Monte Carlo modeling of light transport in multi-layered tissues. *Comput. Meth. Prog. Bio.* **1995**, *47*, 131−146.
(40) Boas, D. A.; Pitris, C.; Ramanujam, N. *Handbook of Biomedical Optics*; CRC Press, 2011.
(41) Glenn, D. R.; Zhang, H.; Kasthuri, N.; Schalek, R.; Lo, P.; Trifonov, A.; Park, H.; Lichtman, J.; Walsworth, R. L. Correlative light and electron microscopy using cathodoluminescence from nanoparticles with distinguishable colours. *Sci. Rep.* **2012**, *2*10.1038/srep00865.
(42) Goetz, J. G.; Minguet, S.; Navarro-Lerida, I.; Lazcano, J. J.; Samaniego, R.; Calvo, E.; Tello, M.; Osteso-Ibanez, T.; Pellinen, T.; Echarri, A. Biomechanical remodeling of the microenvironment by stromal caveolin-1 favors tumor invasion and metastasis. *Cell* **2011**, *146*, 148−163.

DOI: 10.1021/acsphotonics.5b00289
ACS Photonics 2015, 2, 1416−1422